

The study of thermonuclear X-ray bursts in accreting millisecond pulsar MAXI J1816–195 with *NuSTAR* and *NICER*

Manoj Mandal,¹* Sabyasachi Pal,¹† Jaiverdhan Chauhan,²‡ Anne Lohfink,² Priya Bharali³

¹Midnapore City College, Kuturia, Bhadutala, West Bengal, 721129, India

²Department of Physics, Montana State University, P.O. Box 173840, Bozeman, MT 59717-3840, USA

³Mahatma Gandhi Government Arts College, Puducherry, India

Accepted XXX. Received YYY; in original form ZZZ

ABSTRACT

The millisecond pulsar MAXI J1816–195 was recently discovered in an outburst by *MAXI* in 2022 May. We study different properties of the pulsar using data from *NuSTAR* and *NICER* observations. The unstable burning of accreted material on the surface of neutron stars induces thermonuclear (Type-I) bursts. Several such thermonuclear bursts have been detected by MAXI J1816–195 during its outburst. We investigate the evolution of the burst profile with flux and energy using *NuSTAR* and *NICER* observations. During the *NuSTAR* observation, a total of four bursts were detected from the source. The duration of each burst is around ~ 30 s and the ratio of peak to persistent count rate is ~ 26 as seen from the *NuSTAR* data. The burst profiles are modelled using a sharp linear rise and exponential decay function to determine the burst timing parameters. The burst profiles show a relatively long tail at lower energies. The broadband time-resolved spectra during the burst periods are successfully modelled with a combination of an absorbed blackbody along with a non-thermal component to account for the persistent emission. From our modelling results, we are able to estimate the maximum apparent emitting area of the blackbody of the neutron star to be ~ 12.5 km during the peak of the outburst and the maximum distance to the object to be 8.7 kpc. Our findings for the mass accretion rate and the alpha factor indicate the stable burning of hydrogen via a hot CNO cycle during the bursts.

Key words: accretion, accretion discs – stars: neutron – X-ray: binaries – X-rays: bursts – X-rays: individual: MAXI J1816–195

1 INTRODUCTION

MAXI J1816–195, an accreting X-ray pulsar, was discovered by the Monitor of All-sky X-ray Image¹ (*MAXI*; Matsuoka et al. 2009) on 2022 June 7 (Negoro et al. 2022), and has subsequently been followed-up by different multi-wavelength observations (Beauchamp et al. 2022; Bright et al. 2022; Kennea, Evans & Negoro 2022b). Importantly, Bult et al. (2022) found pulsations at 528.6 Hz from MAXI J1816–195 using *NICER*, confirming the nature of the source as an accreting millisecond X-ray pulsar. The timing results revealed that MAXI J1816–195 possesses an orbital period of 4.8 hours (Bult et al. 2022). *NICER* observations also found 15 thermonuclear bursts from the source during the span of its outburst (Bult et al. 2022). The source was also observed by *NuSTAR* and the pulsation at 528 Hz was confirmed, and an X-ray reflection component was found (Chauhan et al. 2022). MAXI J1816–195 was also studied using *Insight*-HXMT and 73 bursts from the source have been detected (Yu-Peng et al. 2022). The broadband persistent spectra were modelled using an absorbed convolution thermal Comptonization component with input seed photons from the accretion disk. During bursts, an absorbed

blackbody model is used to fit the *HXMT* spectra and f_a model is applied to account for the variable persistent emission.

The first thermonuclear (Type-I) X-ray burst in a pulsar was discovered more than 40 years ago in 1976 (Grindlay et al. 1976); it provided a new arena for the study of different parameters of neutron stars (such as mass, radius, spin frequency, photospheric radius expansion; Bhattacharyya 2010). During a Type-I burst, the surface emission is typically more than 10 times brighter than the remaining X-ray emission. As a result, it may be possible to isolate the surface radiation from the total emission and utilize it to accurately determine the neutron star parameters (Bhattacharyya 2010). An X-ray burst is powered by a low-mass companion star from which the neutron star (NS) accretes gas through an accretion disc. Matter gathers on the stellar surface of the neutron stars from the low-mass binary companion. During the burst, thermonuclear burning transforms the accreted hydrogen and helium on the surface of the NS into heavier elements (Lewin, van Paradijs & Taam 1993; Strohmayer & Bildsten 2003; Schatz & Rehm 2006). The burning layer will ignite completely on a time scale of a few seconds and cause a burst if radiative cooling is slower than the energy generation rate.

The rapid increase in the X-ray intensity during a thermonuclear burst is mainly due to the unstable ignition of fuel on the surface of the neutron star (Galloway et al. 2008), which returns to the pre-burst level after a short time by following an exponential decay (Lewin, van Paradijs & Taam 1993; Galloway et al. 2008). During the burst,

* E-mail: manojmandal@mcconline.org.in

† E-mail: sabya.pal@gmail.com

‡ E-mail: jaiverdhan.chauhan@montana.edu

¹ <http://maxi.riken.jp/top/index.html>

the rapid flux rise happens in a short period of 0.5–5 s and the decay happens over 10–100 s (Lewin, van Paradijs & Taam 1993; Bhattacharyya 2010). To date, Type-I bursts have been found in more than 100 sources (Liu et al. 2007). Not all bursts have the same burst profile, both single and multi-peaked burst profiles have been reported depending on the source. Single-peaked bursts are typically observed in most of the thermonuclear bursts but double-peaked bursts are observed for several sources like GX17+2 (Kuulkers et al. 2002), 4U 1709–267 (Jonker et al. 204), 4U 1636–53 (Watts & Maurer 2007), and 4U 1608–52 (Penninx et al. 1989), MXB 1730–335 (Bagnoli et al. 2014). Triple-peaked bursts are relatively rare to observe, and observed in 4U 1636–53 (van Paradijs et al. 1986; Zhang et al. 2009). Li et al. (2021) found several multi-peaked Type-I bursts from 4U 1636–536 using *RXTE*, and an extraordinary quadruple-peaked burst was also observed for the same source.

At higher energies, double-peaked profiles were observed for several sources due to photospheric expansion when the peak flux reached the Eddington luminosity (Lewin, van Paradijs & Taam 1993). Near a constant luminosity (L), the photospheric radius (R) increases and the effective temperature decreases as, $T_{\text{eff}} = \left(\frac{L}{4\pi\sigma}\right)^{1/4} R^{-1/2}$ (Lewin, van Paradijs & Taam 1993). The time-resolved continuum spectra are modelled with an absorbed blackbody component by assuming the entire surface of the neutron star emits like a blackbody (van Paradijs 1978; Kuulkers et al. 2003). The Eddington limit may be reached at the peak of the burst, which would result in extremely high radiation pressure and allow the expansion of the photosphere of the neutron star (Tawara et al. 1984). The blackbody radius continues to increase during the rising phase of a burst, reaching a maximum value. The photospheric radius started to decrease during the decay phase of the burst. This process continues until the photospheric radius reaches its original value and the neutron star surface starts cooling. At the end of the process, the photospheric radius becomes equal to the radius of the neutron star, and at the touchdown phase, the temperature has the highest value along with a lower blackbody radius (Lewin, van Paradijs & Taam 1993; Kuulkers et al. 2003). The radius of a neutron star can be measured using time-resolved spectroscopy during the thermonuclear burst (during the cooling phase after the touchdown; Lewin, van Paradijs & Taam 1993; van Paradijs 1978; Galloway et al. 2008). The blackbody temperature shows two maxima in the temperature profile during the Type-I burst, the second maxima implies the touchdown phase (Galloway et al. 2008). Previously, Type-I X-ray bursts were observed from GRS 1741.9–2853 during the outburst of May 2020 using *NuSTAR* which revealed multi-peaked bursts and a photospheric radius expansion (PRE) during the peak of the burst (Pike et al. 2021).

Previous work has shown that the count rate, blackbody temperature, and apparent emitting area of the blackbody showed significant variation during the X-ray bursts in several sources. It is this variability that can be used to estimate the evolution of the photosphere radius of the neutron star. The time-resolved spectroscopy of GX 3+1 using *Astrosat* observations suggested that there was a photospheric radius expansion for this source during the rising phase of the burst and, using the burst parameters, the source distance was estimated to be ~ 9.3 kpc (Nath et al. 2022). During the decay phase of an X-ray burst, the photospheric radius decreases and reaches a value of ~ 6.81 km. Time-resolved spectroscopy was performed for 4U 1636–536 using *Astrosat* data, which indicated an expansion of the photospheric radius during an X-ray burst (Beri et al. 2019). Devasia, Raman, & Paul (2021) studied time-resolved spectroscopy for the source Cyg X-2 using the *Astrosat* observations, which suggested that the black-

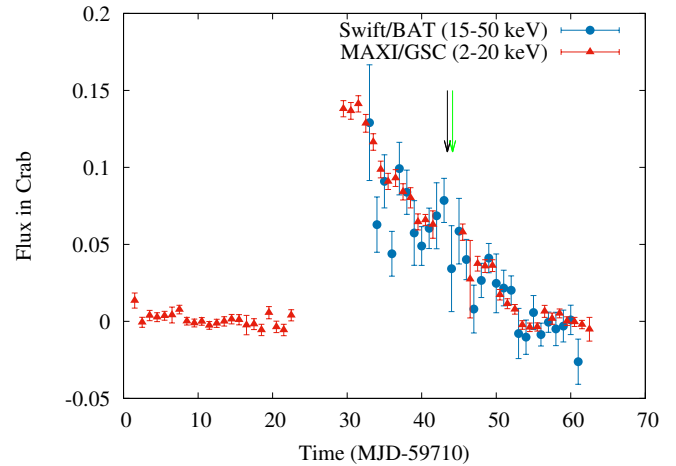


Figure 1. An outburst is detected from MAXI J1816–195 using *Swift*/BAT and *MAXI*/GSC during 2022 May–June. The black arrow indicates the time of the *NuSTAR* observation, and the green arrow represents the simultaneous *NICER* observation time, respectively. *NuSTAR* observed the source during the decay phase of the outburst.

body flux and radius increased in the rising phase of the X-ray burst and that at the same time, the blackbody temperature dropped. The blackbody radius and flux decreased in the decay phase of the burst, and the blackbody temperature increased during the decay of the X-ray burst. Thermonuclear bursts can therefore be used to probe several properties of a source during the burst, including the temperature profile, apparent emitting area of the blackbody, photosphere expansion, and emission mechanism.

We observed MAXI J1816–195 during the May 2022 outburst using *NuSTAR*, which has a good sensitivity up to ~ 79 keV. The detailed timing and spectral study of MAXI J1816–195 is used to investigate crucial information about the source by using simultaneous *NICER* and *NuSTAR* observations. In this paper, we study the timing and spectral properties of MAXI J1816–195 using data from *NuSTAR* and *NICER* observatories. We have analyzed each burst spectra separately instead of stacking, as the burst profiles seem to be slightly different from each other. We have analyzed two broadband pre and post-burst spectra which are simultaneous with *NuSTAR* and *NICER*. During the thermonuclear burst, time-resolved spectroscopy is performed using *NICER*. This paper is organized as follows: The observational data and reduction procedure are described in Section 2. Section 3 summarises the results of spectral and timing analysis. In Section 4, we discuss the results obtained. The findings of the study are summarised in Section 5.

2 DATA ANALYSIS AND METHODOLOGY

We analyzed data taken by *NuSTAR* and *NICER* covering the entire duration of the outburst, starting from May 2022 and lasting for nearly two months. We reduced data from the two satellites using HEASOFT version 6.28. We also used final data products (light curves) provided by *MAXI* and the Burst Alert Telescope onboard Neil Gehrels Swift Observatory² (Krimm et al. 2013) missions.

² <https://swift.gsfc.nasa.gov/results/transients/>

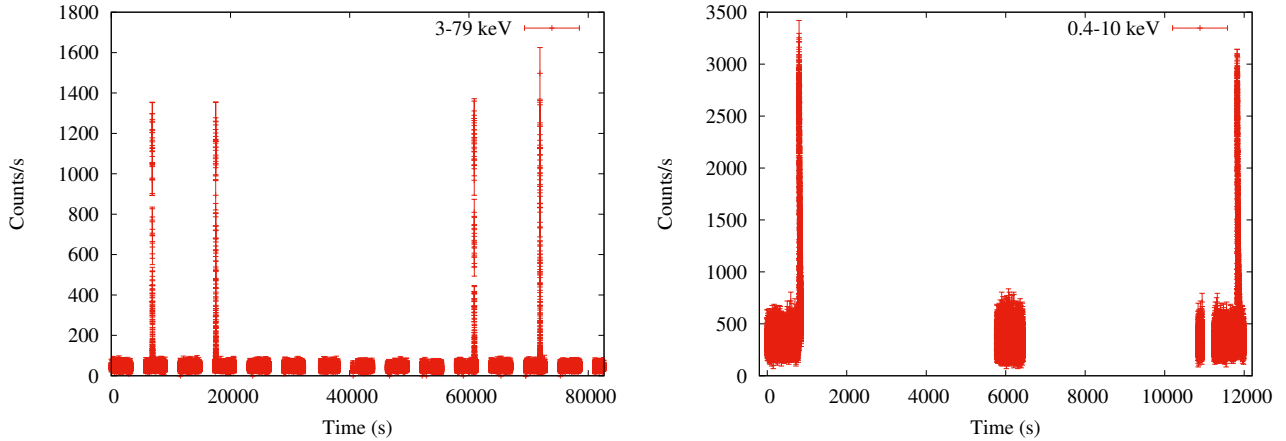


Figure 2. The left-hand side panel shows the *NuSTAR*-FPMA 1 s binned background corrected light curve in the energy range of 3–79 keV, showing four thermonuclear bursts. The right-hand side panel represents the *NICER* (0.4–10 keV) 1 s binned light curve (Obs. ID–533011601) during the simultaneous observation with *NuSTAR*. The *NICER* light curve shows two bursts, which are also detected with *NuSTAR*. The third and fourth bursts in the *NuSTAR* light curve are common with the two *NICER* bursts.

2.1 *NuSTAR* observation

The Nuclear Spectroscopic Telescope Array (*NuSTAR*) consists of two identical X-ray telescope modules that are co-aligned and operate in a broad energy range of 3–79 keV. Each detector of each telescope (typically known as focal plane modules A (FPMA) and B (FPMB)) provides a spectral energy resolution of 400 eV (FWHM) at 10 keV (Harrison et al. 2013). *NuSTAR* performed an observation of MAXI J1816–198 on 2022 June 23–24 with an exposure of ~35 ks. The data were reduced using the NuSTARDAS pipeline provided under HEASOFT with CALDB version of 20221130. The data was screened and calibrated using NUPIPELINE. The source light curves and spectra were extracted using a circular region of radius 60 arcsec centred at the source position using NUPRODUCTS scripts provided by the NuSTARDAS pipeline. The background light curves and spectra were extracted from circular regions 100 arcsec away from the source. The background correction of the light curve was made using 1cmath.

2.2 *NICER* observation

A soft X-ray non-imaging spectroscopy and timing instrument, the Neutron Star Interior Composition Explorer (*NICER*) is located on the International Space Station. The main component of *NICER* is the X-ray Timing Instrument (XTI), which operates in the soft X-ray range of 0.2–12 keV (Gendreau et al. 2016). A series of follow-up observations of MAXI J1816–195 was taken with *NICER* beginning in 2022 May. We have used a single *NICER* observation (Obs. ID–5533011601) with exposure of ~2.33 ks which was simultaneous with *NuSTAR* observation. *NICERDAS* in HEASOFT was used to process the raw data. By applying the standard calibration and filtering tool `nicer12` to the raw data, we produced clean event files. We used `XSELECT` to extract light curves and spectra for MAXI J1816–195 from the clean event files. We chose good time intervals for the timing analysis based on the following criteria: the ISS was not in the South Atlantic Anomaly (SAA) region, the source direction was at least 30° away from the bright Earth, and the source elevation was greater than 20° above the Earth’s limb. We used the task `barycorr` to apply barycentric corrections for the time analysis. Light curves with a time resolution of 1 s containing events in the 0.4–10 keV are generated for timing analysis. We have analyzed the *NICER* data

with the CALDB version of 20210707. The `nibackgen3C503` tool was used to simulate the background for each observational epoch (Remillard et al. 2021).

3 RESULTS

The millisecond pulsar MAXI J1816–195 was discovered by *MAXI* during an outburst in 2022 May. Several follow-up observations have been conducted to study the source’s multi-wavelength behaviour (Bult et al. 2022; Kennea, Evans & Negoro 2022b; Chauhan et al. 2022; Kennea, Evans & Negoro 2022a; de Martino et al. 2022; Bright et al. 2022; Beauchamp et al. 2022). For example, we used the *Swift*/BAT telescope’s high energy X-ray coverage (15–50 keV) and daily monitoring of the entire sky, to ascertain the spectral state of the source and duration of the outburst. Fig. 1 shows the outburst from MAXI J1816–195 during 2022 May–June as seen with *MAXI* and *BAT*. The outburst from MAXI J1816–195 continued for nearly 30 days. The maximum flux reached by the source was ~0.15 crab as observed with *Swift*/BAT (15–50 keV) on 2022 June 13 (MJD 59743). Simultaneous observation with *NuSTAR* and *NICER* was conducted on 2022 June 24 and is the focus of this paper. The observation time is indicated using two arrows in Fig. 1. It is clear from the figure, that the simultaneous *NICER*/*NuSTAR* observation was performed in the decay phase of the outburst. The source was detected using *NuSTAR* at the location of RA = $18^h 16^m 52^s .40$, Dec = $-19^\circ 37' 58'' .35$, and the source is 1.45 arcsec away from the *Swift*/XRT localization (Kennea, Evans & Negoro 2022b), which is within the 2.2 arcsec (90 per cent confidence) error radius of the XRT position of the source.

3.1 X-ray bursts and burst timing analysis

Multiple thermonuclear bursts are found from MAXI J1816–195 during the outburst of 2022 using *NuSTAR* and *NICER*. The X-ray bursts were detected by the *NuSTAR* observation on 2022 June 23. The left-hand side panel of Fig. 2 shows the light curve (3–79 keV) using *NuSTAR*/FPMA, which shows four bursts during the observation. The

³ https://heasarc.gsfc.nasa.gov/docs/nicer/tools/nicer_bkg_est_tools.html

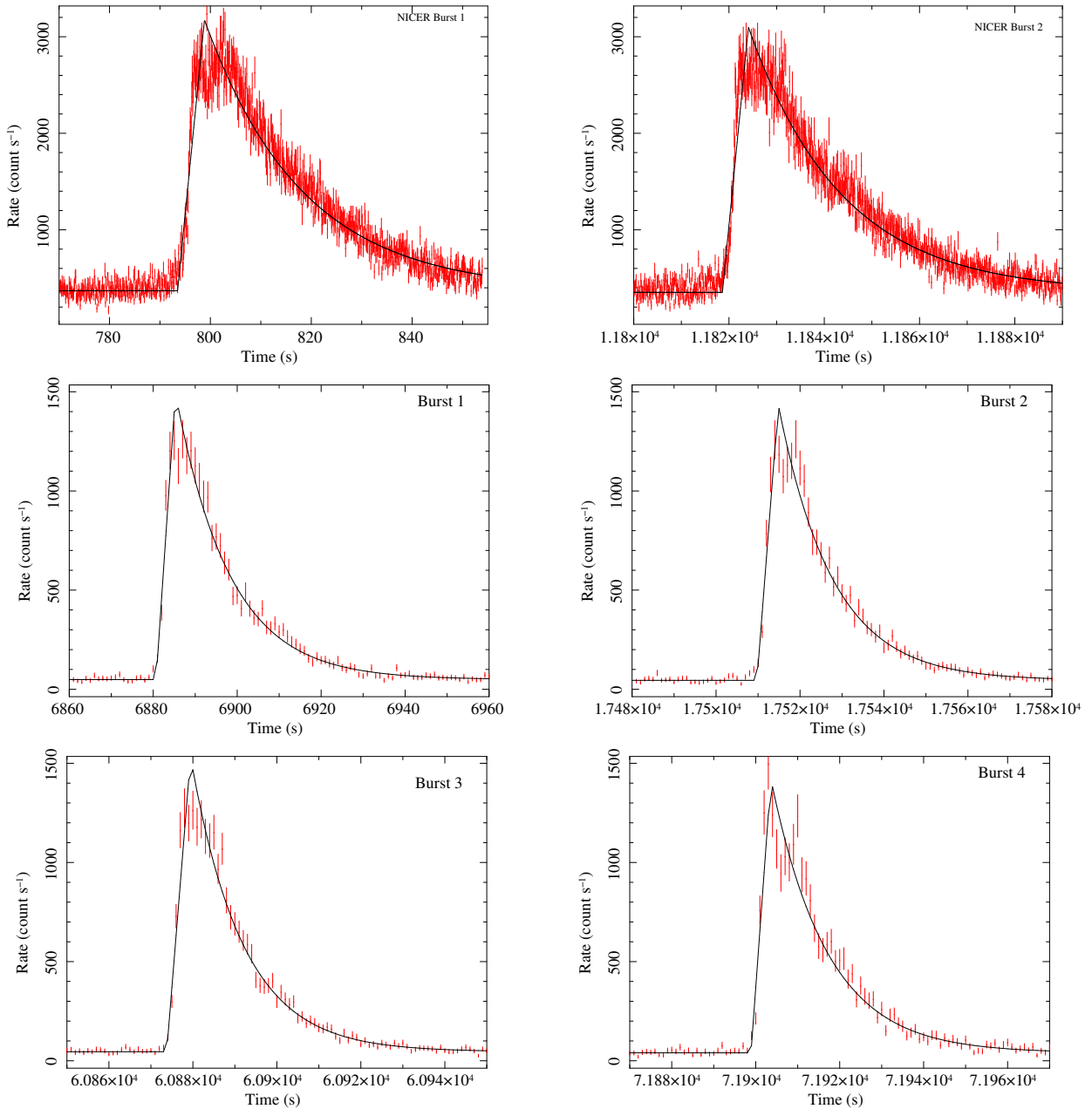


Figure 3. Modelling of four X-ray bursts detected from MAXI J1816–195 using *NuSTAR* and *NICER*. The burst profiles are modelled with the *burs* model (a linear rise and an exponential decay) and the best-fitting parameters are summarised in Table 2. Two thermonuclear bursts are detected from MAXI J1816–195 with *NICER* (0.4–10 keV) using 1 s binned light curve (Obs. ID–5533011601), shown in the top left and top right-side images of the figure. The rest of the four images represent thermonuclear bursts, which are detected from *NuSTAR* observation. The duration of each burst is nearly 30 s.

Table 1. Details of X-ray bursts detected from MAXI J1816–195 using *NuSTAR* and *NICER* observations.

Instrument	Start time (MJD)	Number of bursts	Obs. ID
<i>NuSTAR</i>	59753.45	4	90801315001
<i>NICER</i>	59754.14	2	5533011601

average peak count rate of the bursts was estimated as ~ 1300 counts s^{-1} from *NuSTAR*/FPMA. The right-side panel of Fig. 2 shows the

light curve of the source using *NICER*, which indicates two thermonuclear bursts with a peak count rate of ~ 3000 counts s^{-1} during simultaneous observation with *NuSTAR*. The summary of detected bursts from MAXI J1816–195 is given in Table 1. The peak count of burst 1, burst 2, and burst 3 was ~ 1260 counts s^{-1} and the duration of the bursts was ~ 30 s. For burst 4, the peak count was ~ 1500 counts s^{-1} with a burst duration of ~ 30 s. The right-hand side image of Fig. 2 shows the light curve using *NICER*, which is simultaneous with *NuSTAR*. The simultaneous observations of the source using *NICER* (Obs. ID–5533011601) and *NuSTAR* (Obs. ID–90801315001) implies that the burst 3 and burst 4 of *NuSTAR* are simultaneous with *NICER* bursts (Fig. 2). For the *NuSTAR* observation, the recurrence time between bursts 1 and 2 was roughly 10.64 ks, and the recurrence

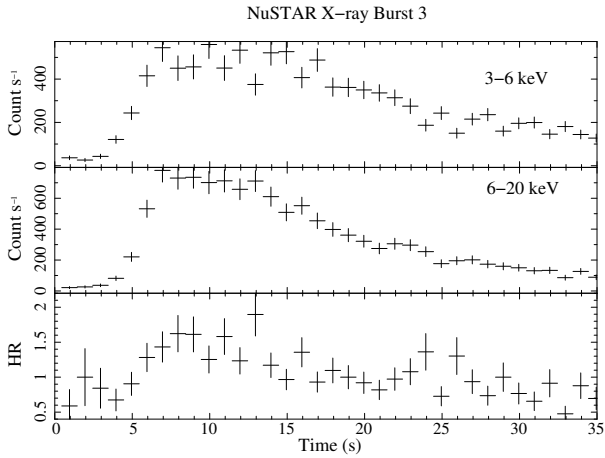


Figure 4. Evolution of hardness ratio of MAXI J1816–195 using *NuSTAR* during a thermonuclear burst. *NuSTAR* detected a total of four bursts during the observation and this HR is shown for the third burst. The HR for the rest of the three bursts is shown in Fig. A1. The first and second panels show the 1 s binned light curve in the energy band of 3–6 keV and 6–20 keV, respectively. The bottom panel shows the variation of the hardness ratio (6–20 keV)/(3–6 keV). The hardness ratio evolved with the burst and reached a maximum value of ~ 2 during the peak of the burst.

time between bursts 3 and 4 was approximately 11.03 ks (the data gap between two consecutive bursts was ~ 5.5 ks). The recurrence time for two successive bursts for the *NICER* observation was ~ 11 ks (the data gap between two consecutive bursts was ~ 10 ks).

The *NuSTAR* burst profiles are modelled using the QDP model bursts shown in Fig. 3. The characteristics of Type-I bursts can be modelled using the fast linear rise and exponential decay profile. The burst profiles are fitted with a constant and the burst model (linear rise and exponential decay). The *NuSTAR* X-ray burst fitting parameters imply a sharp rise time (4.6 s to 7.6 s) and a slow decay duration of 12.3 to 13.4 s. The X-ray bursts detected using *NuSTAR* indicate that the peak count rates are around 26 times higher than the persistent levels. The *NICER* burst profiles are also fitted with the same model bursts and the best-fitting parameters are summarised in Table 2. Fig. 3 shows two bursts using *NICER* data in the 0.4–10 keV energy band during the simultaneous observation with *NuSTAR*. The duration of the burst was nearly 30 s, and the pattern was a sharp linear rise in flux and comparatively slow exponential decay. The *NICER* X-ray burst fitting parameters for *NuSTAR* indicate a rapid rise time of 5.5–5.8 s and a gradual decline time of ~ 19 s. The burst duration was around 35 s. The peak count rates are ~ 7.5 times higher than the persistent levels.

3.2 Evolution of hardness ratio

We begin by studying the variation of the hardness ratio during the thermonuclear bursts using *NuSTAR*. The light curves in two energy bands, 3–6 keV and 6–20 keV, are produced during the burst with a time resolution of 1 s. The bottom panel of Fig. 4 shows the evolution of the hardness ratio (6–20 keV)/(3–6 keV) during the thermonuclear burst as observed with *NuSTAR*. The HR is shown for the *NuSTAR* burst-3. Initially, the hardness increases from 0.5 to a peak of about 1.5. The HR gradually decreases and returns to a persistent level, as the burst flux begins to decrease. The hardness ratio shows a similar pattern for all four X-ray bursts during the *NuSTAR* observation.

3.3 Energy-resolved burst profiles

We have studied the energy dependence of the burst profiles of MAXI J1816–195 using simultaneous *NuSTAR* and *NICER* data during the outburst. The top left and top right-side images of Fig. 5 show the energy-dependent burst profiles using *NICER*. The burst profiles are generated for the energy ranges of 0.4–3 keV, 3–5 keV, and 5–10 keV for two different bursts during the *NICER* observation. Fig. 5 shows that the peak count rate decreases with an increase in energy, and the peak count rate in the higher energy band 5–10 keV is ~ 2.5 times less compared to 0.4–3 keV energy band. The *NICER* burst profiles significantly evolved with energy, and during the decay phase of the burst, a comparatively long tail is seen in the burst profile at low energy.

The energy dependence of the burst profiles is also observed from the *NuSTAR* observation. Fig. 5 shows burst profiles at different energies (3–6 keV, 6–10 keV, 10–20 keV) using *NuSTAR*/FPMA data. The X-ray bursts are detected in different energy bands of *NuSTAR*. It is visible that the peak fluxes of bursts evolve with energy, and with increasing energy, the amplitude of the burst peak count rate decreases. The energy-resolved bursts are significantly detected up to 20 keV using *NuSTAR*. The peak count rate of the burst profile is reduced by a factor of ~ 4 in the higher energy band (10–20 keV) compared to the lower energy band (3–6 keV). A relatively large tail is found in the low energy range (3–6 keV) compared to the high energy range (10–20 keV) during the burst decay phase. The variation of the hardness ratio is also investigated to look for the evolution of the source state during the burst. Fig. 4 represents the evolution of the hardness ratio for burst-3 using the *NuSTAR* observation. The variation of the hardness ratio shows a similar trend for all four bursts during *NuSTAR* observation. During the rising phase of the burst, hard photons (6–20 keV) dominate the soft band photons (3–6 keV) as HR increases till the peak of the burst. In the decay phase of the burst, the HR decreases and the soft photons dominate over the hard photons.

3.4 Time-resolved burst spectroscopy

To understand the dynamic evolution of observed thermonuclear bursts, we performed time-resolved spectroscopy and studied the variation of different spectral parameters during the burst. The pre and post-burst spectra for MAXI J1816–195 are obtained from the joint analysis of the *NICER* and *NuSTAR* data and modelled in XSPEC (Arnaud 1996). The joint pre and post-burst spectra (0.5–79 keV) are obtained for a time bin of ~ 300 s. We used only *NICER* data (0.5–10.0 keV) to extract time-resolved burst spectra. A total of 25 spectra (P1 to P25) are generated for each burst, P1 and P25 are the pre and post-burst spectra, and the rest of them (P2 to P24) are during the burst. Two different time bins are taken to extract the time-resolved spectra. We selected a time bin of 2 s to extract the spectra from P2 to P18 and a time bin of 4 s from P18 onward. To optimize the signal-to-noise ratio in the burst’s decaying portion, we extended the time bin from 2 s to 4 s.

The pre and post-burst spectra are described by the thermal Comptonization XSPEC model *nthComp* (Zdziarski et al. 1996; Zycki et al. 1999) along with a disc (*diskbb*) component. The interstellar medium absorption is accounted for by the TBABS (Wilms, Allen & McCray 2000) model in XSPEC. The best-fit broadband pre-burst spectra are shown in Fig. 6 using the simultaneous observation of *NuSTAR* and *NICER* during burst 3 and burst 4 respectively. The results of the pre and post-burst spectral fitting are summarised in Table 3. The average hydrogen column density (N_H) from the pre

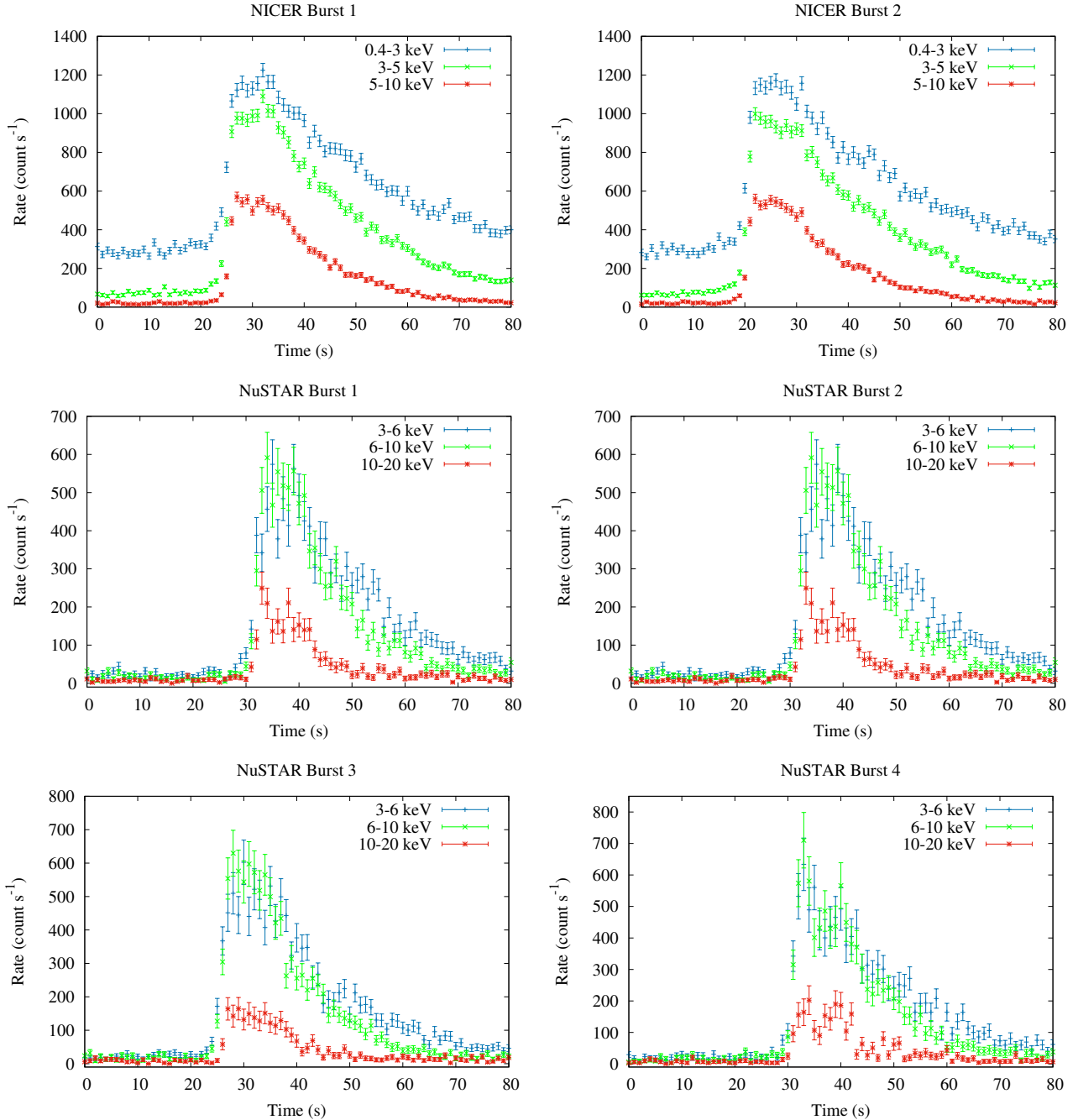


Figure 5. Energy-resolved burst profiles are shown using *NICER* and *NuSTAR*/FPMA simultaneous observation data. The top left and right-hand side panels show energy-resolved burst profiles for MAXI J1816–195 using *NICER* with a 1-s binned light curve (Obs. ID–5533011601) and the rest of the bursts are observed using *NuSTAR*. Four thermonuclear bursts are detected from MAXI J1816–195 using *NuSTAR* 1 s binned light curves. The burst profiles show a comparatively lower peak count rate at higher energy bands. Each burst is continued for nearly 30 s. The bursts are detected significantly up to an energy of 20 keV using *NuSTAR*.

and post burst spectra was $\sim 2.38 \times 10^{22} \text{ cm}^{-2}$. The photon index shows a consistent value of ~ 2 for the pre-burst and post-burst intervals. The joint spectral modelling provides an electron temperature of $\sim 11 \text{ keV}$ for the P1 phase of each burst. The lower value of the electron temperature during the pre-burst time implies the source is in the soft state.

We divide both the bursts into 23-time bins, namely; P2 to P24. The P2 and P3 time intervals correspond to the sharp rise, whereas

time bin P4 signifies the peak of the thermonuclear burst (TNB). We further broke the exponential decay part of the TNB into 19 parts, which are represented by the time bins P5 to P24. We have selected a time bin of 2 s for the first 17 points (P2 to P18) and the time bin increased to 4 s for the rest of the burst (P19 to P24). For each interval, the spectra are extracted through XSELECT using the good time interval files (GTIs) for each burst for *NICER* data.

The *NICER* time-resolved spectra were modelled using the combi-

Table 2. Fitting parameters of X-ray bursts using the QDP model bursts from simultaneous *NuSTAR* observation (Obs. ID - 90801315001) and *NICER* observation (Obs. ID - 5533011601).

Burst No. <i>NuSTAR</i>	Burst start time (s)	Burst duration (s)	Peak to persistent count rate	Duration of rising (s)	Duration of decay (s)	Peak count rate (count s ⁻¹)
1	6880	~30	~26.2	~4.6	12.8 ± 0.5	1259 ± 91
2	17510	~30	~26.1	~7.6	12.5 ± 0.1	1256 ± 94
3	60875	~30	~26.5	~5.7	12.3 ± 0.4	1273 ± 98
4	71900	~25	~31.3	~4.7	13.4 ± 0.5	1503 ± 121
<i>NICER</i> burst 1	795	~35	~7.7	~5.8	19.1 ± 0.8	3100 ± 60
<i>NICER</i> burst 2	11820	~35	~7.4	~5.5	19.6 ± 0.8	2970 ± 40

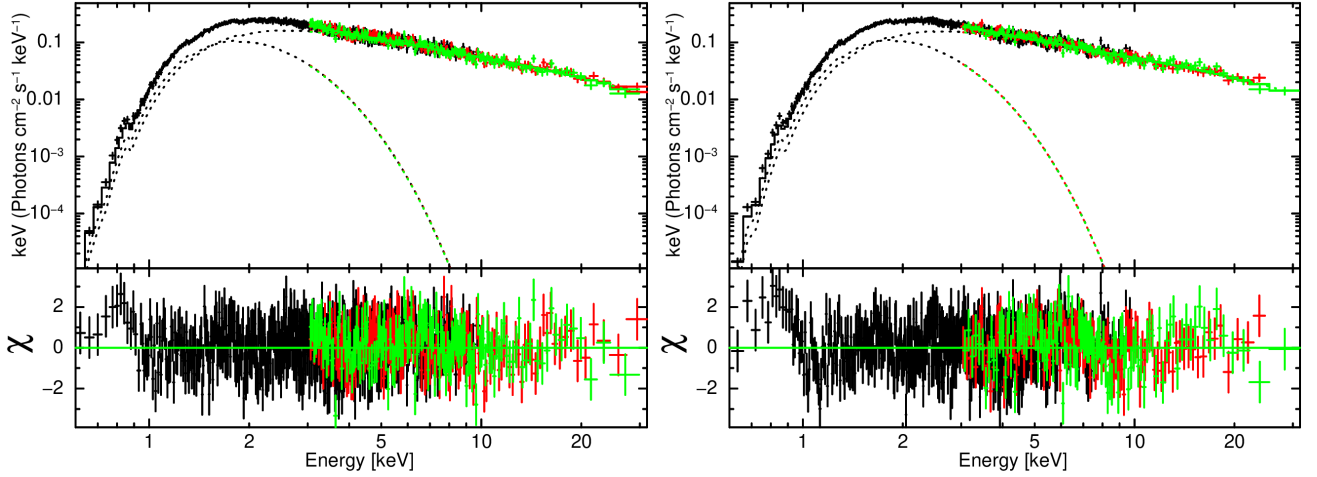


Figure 6. The plots highlight the fitted spectra using simultaneous *NICER/NuSTAR* data of the thermonuclear burst-3 and burst-4 for the initial persistent time bin P1. The best-fit model is $\text{TBabs} \times (\text{diskbb} + \text{nthComp})$. The fitting model and strategy are discussed in Section 3.4. The best-fitting parameters are presented in Table 3.

nation of absorbed blackbody along with a non-thermal component to account for the persistent emission. The burst spectra are fitted with a combination of galactic absorption, a blackbody (`bodyrad`) model, and the persistent spectrum during the burst is accounted for using the f_a method (Worpel, Galloway & Price 2013). The best-fitting results of time-resolved spectra are summarised in Table A1. During the decay phase (P22 to P24) of the TNB 3, the signal-to-noise ratio was low and fitting statistics were not good, we have not added this in Table A1. The hydrogen column density is fixed to the average value of pre-burst and post-burst level $\sim 2.38 \times 10^{22} \text{ cm}^{-2}$ during the fitting of the *NICER* time-resolved spectra. The dimensionless f_a parameter evolves during the burst as the persistent emission shows variation during this time (Worpel, Galloway & Price 2013). We look for the variation of the persistent emission during the burst through the f_a method. We have applied the f_a method to account for the non-thermal emission for the time-resolved spectra (P2–P24). The f_a value does not show significant variation during the burst and f_a reached a maximum of 1.74 ± 0.21 for burst 3 at the peak of the burst (P4 phase). Compared to traditional methods, the flux value in the f_a method is lower around the peak of the burst. The variation of different spectral parameters during the burst is shown in Fig. 7. The top panel of Fig. 7 shows the variation of the blackbody temperature; the second panel shows the variation of the blackbody normalization; the third and fourth panels show the evolution of the total flux and blackbody flux, respectively. The bottom panel of Fig. 7 shows the evolution of the persistent flux of the source. The blackbody temperature varies between 1.03 keV, and 2.16 keV during burst 3 and

for burst 4, kT varies between 0.82 keV to 2.09 keV. The blackbody temperature attains its maximum value of 2.16 keV during the peak (P4) of the burst and the normalization of the blackbody was ~ 207 for burst 3. From the normalization, the blackbody radius (R_{bb}) can be estimated via, $\text{Norm}_{\text{bb}} = \frac{R_{\text{bb}}^2}{D_{10}^2}$, where D_{10} is the source distance in units of 10 kpc. A peak flux of $\sim 4.2 \times 10^{-8} \text{ erg cm}^{-2} \text{ s}^{-1}$ is reached during the P4 phase of burst 3. The apparent emitting area of the blackbody is estimated from the average normalization of the blackbody component for burst 3 and burst 4 during the P4 phase. The apparent emitting area of the blackbody corresponding to the normalization ~ 212 is estimated to be $\sim 9.2 \text{ km}$ (assuming the source distance is $\sim 6.3 \text{ kpc}$ (Chen et al. 2022)) and $\sim 12.5 \text{ km}$ (assuming the source distance is $\sim 8.6 \text{ kpc}$ (Bult et al. 2022)) respectively.

4 DISCUSSION

We present the timing and spectral study of the newly discovered millisecond pulsar MAXI J1816–195 using *NuSTAR* and *NICER* data. The *NuSTAR* light curve shows four X-ray bursts and the duration of each burst was around 30 s. At higher energies, the burst decays faster, which suggests that the temperature is falling as the burst evolves. Earlier, a similar type of trend was observed for several other sources, for example, 4U 1636–536 and GX 3+1 (Beri et al. 2019; Nath et al. 2022). The burst profiles for MAXI J1816–195 depend strongly on energy, and during the decay phase of the burst,

Table 3. Best-fitting parameter values [XSPEC model TBabs \times (diskbb \times nthComp)] of the ~ 300 s pre-burst and post-burst *NICER* and *NuSTAR* joint spectra of burst 3 and burst 4 from MAXI J1816–195.

Components	Parameters	Pre-burst P1 (373 s)	Post-burst P25 (242 s)
Burst 3			
TBABS	N_{H} ($\times 10^{22} \text{ cm}^{-2}$)	2.39 ± 0.04	2.36 ± 0.56
diskbb	T_{in} (keV)	0.5 ± 0.02	0.7 ± 0.25
	Norm.	1428^{+296}_{-231}	237^{+1857}_{-145}
nthComp	Γ	2.0 ± 0.04	$2.1^{+0.03}_{-0.25}$
	kT_e (keV)	$11.2^{+8.9}_{-2.6}$	1000^{\pm}
	Norm. ($\times 10^{-1}$)	4.0 ± 0.3	$5.7^{+1.8}_{-3.0}$
	F_{Total} ($\times 10^{-9} \text{ ergs cm}^{-2} \text{ s}^{-1}$)	4.3 ± 0.04	6.1 ± 0.60
	F_{diskbb} ($\times 10^{-9} \text{ ergs cm}^{-2} \text{ s}^{-1}$)	1.4 ± 0.08	0.6 ± 0.30
	F_{nthComp} ($\times 10^{-9} \text{ ergs cm}^{-2} \text{ s}^{-1}$)	3.0 ± 0.06	5.2 ± 0.70
	χ^2/dof	803.13/799	210.30/209
Burst 4			
		P1 (350 s)	P25 (322 s)
TBABS	N_{H} ($\times 10^{22} \text{ cm}^{-2}$)	2.42 ± 0.04	2.37 ± 0.07
diskbb	T_{in} (keV)	0.5 ± 0.02	0.5 ± 0.03
	Norm.	1440^{+306}_{-237}	990^{+330}_{-225}
nthComp	Γ	2.0 ± 0.05	2.1 ± 0.05
	kT_e (keV)	$11.7^{+21.48}_{-3.29}$	$32.3^{+}_{-21.05}$
	Norm. ($\times 10^{-1}$)	3.9 ± 0.4	4.3 ± 0.54
	F_{Total} ($\times 10^{-9} \text{ ergs cm}^{-2} \text{ s}^{-1}$)	4.3 ± 0.05	4.6 ± 0.08
	F_{diskbb} ($\times 10^{-9} \text{ ergs cm}^{-2} \text{ s}^{-1}$)	1.4 ± 0.08	1.2 ± 0.11
	F_{nthComp} ($\times 10^{-9} \text{ ergs cm}^{-2} \text{ s}^{-1}$)	2.9 ± 0.07	3.2 ± 0.12
	χ^2/dof	745.65/719	622.81/585

*: All the errors are 90% significant and calculated using the MCMC approach in XSPEC

**: All the flux values are unabsorbed and calculated for the energy band 0.5–79 keV

a relatively long tail is observed in the burst profile at lower energies. The energy dependence of the burst profiles implies a softening of X-ray burst spectra in the decay phase of the burst due to the cooling of the photosphere of the neutron star (Lewin, van Paradijs & Taam 1993). This is evident from the hardness ratio's significant evolution. During the rising phase, the hardness ratio increases until it reaches its maximum near the peak of the outburst and has started to decrease in the decay phase of the burst and returns to the persistent level.

The burst profile shows a sharp rise and comparatively slow exponential decay. The *NuSTAR* burst profiles indicate that the peak flux in 3–79 keV increased by a factor of ~ 26 compared to the persistent level during the bursts. The energy resolved burst profiles for *NICER* data are estimated for the energies of 0.4–3 keV, 3–5 keV, and 5–10

keV (Fig. 5), which show that the burst peak count rate reached nearly $1200 \text{ counts s}^{-1}$ in the 0.4–3 keV energy band and above 3 keV the burst peak count rates decay as expected for the Type-I X-ray burst. Earlier, Cyg X–2 showed that the peak count rate was maximum in the energy band of 3–6 keV, and above this, the count rates started to decrease, which suggests a Type-I X-ray burst (Devasia, Raman, & Paul 2021). The burst decay time gradually decreases with the increase in energy, which implies a decrease in temperature due to the cooling of burning ashes with the decay of the burst (Degenaar et al. 2016). The *NuSTAR* energy-resolved burst profiles are generated for energy ranges of 3–6 keV, 6–10 keV, and 10–20 keV (Fig. 5), which show that the count rate reached $600 \text{ counts s}^{-1}$ in the energy band of 3–6 keV, and beyond 6 keV, the peak count rate has

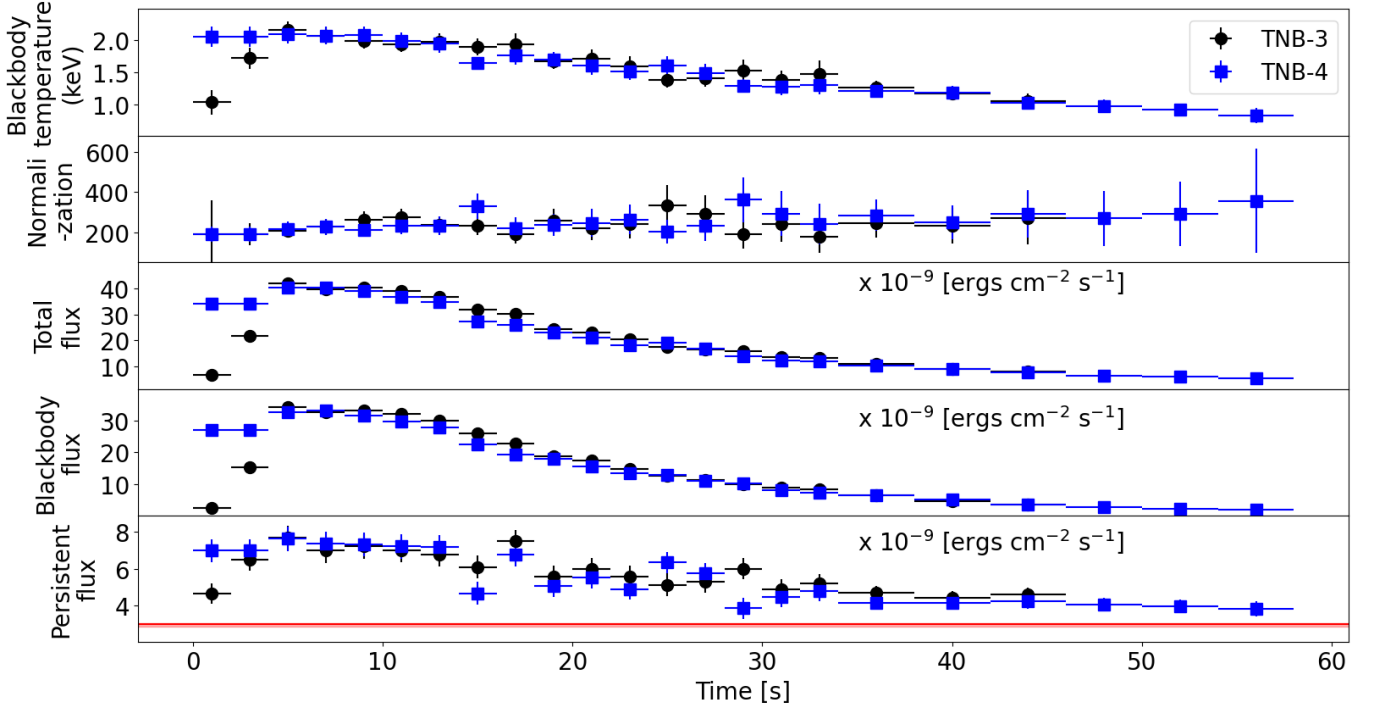


Figure 7. The evolution of the various spectral parameters during the evolution of the TNB: blackbody temperature (kT; Top panel), blackbody normalization (second panel), total flux (third panel), blackbody flux (fourth panel), and persistent flux (bottom panel). The X-axis presents the time from the rise of the TNB. The red horizontal line in the bottom panel highlights the average persistent flux (non-thermal) during the pre-burst time.

started to decrease. In the higher energy band (10–20 keV), the peak count rate decreased to ~ 200 counts s^{-1} . The burst decays faster in a higher energy range, which implies that the temperature decrease as the burst evolves.

Time-resolved spectroscopy during the X-ray burst is crucial as different spectral parameters show significant evolution during the burst. Time-resolved spectroscopy was performed earlier for several sources to understand the accretion mechanism and variation of several spectral parameters during the burst. The time-resolved spectra for MAXI J1816–195 are described using a blackbody and an absorption component along with a non-thermal component. The blackbody temperature reached a maximum of ~ 2 keV near the peak of the burst. The apparent emitting area of the blackbody has reached a maximum of ~ 9.2 km and ~ 12.5 km at the peak of the burst assuming a source distance of 6.3 kpc and 8.6 kpc respectively. Earlier, the MAXI J1816–195 was monitored by *Insight/HXMT*, and a detailed study was conducted by [Chen et al. \(2022\)](#). Using *Insight/HXMT* observation of the source during the time the source was brightest, the photospheric radius expansion was not evident and the peak flux was estimated to be $\sim 8.03 \times 10^{-8}$ erg cm^{-2} s^{-1} and the temperature and apparent emitting area of the blackbody reached the highest value of ~ 2 keV and ~ 11 km respectively ([Chen et al. 2022](#)). An upper limit of source distance of 6.3 kpc was given by [Chen et al. \(2022\)](#) assuming the Eddington luminosity of 3.8×10^{38} erg s^{-1} ([Kuulkers et al. 2003](#)). Similarly, the time-resolved spectral analysis from *NICER* data for this source revealed that the expansion of photosphere expansion was not evident as the typical blackbody temperature and normalization were ~ 1.9 keV and ~ 300 at 10 kpc respectively ([Bult et al. 2022](#)). The blackbody flux varies between $\sim (0.2–3.4) \times 10^{-8}$ erg cm^{-2} s^{-1} during the bursts. The f_a parameter varies between 1–1.7 and 0.8–1.7 for burst 3 and burst 4 respectively, which implies that the contribution of the persistent component from the non-thermal

emission of the burst does not enhance during the peak of the burst. The flux from the non-thermal emission (f_a method) varies between $\sim (4.4–7.6) \times 10^{-9}$ erg cm^{-2} s^{-1} for burst 3. The unabsorbed flux near the peak is $\sim 4.2 \times 10^{-8}$ erg cm^{-2} s^{-1} , which is ~ 11 times higher than the persistent level. The non-burst persistent emission from the source is described with the disc blackbody model along with the thermally comptonized continuum model. The non-burst persistent emission flux of the blackbody and comptonized component are 1.4×10^{-9} and 2.9×10^{-9} erg cm^{-2} s^{-1} respectively, during the pre-burst interval. The upper limit on the source distance can be estimated using the peak flux during the burst.

The unabsorbed blackbody flux during the peak of the burst was $F_{max} = 3.4 \pm 0.15 \times 10^{-8}$ erg cm^{-2} s^{-1} . The source distance can be estimated using this value of Eddington luminosity using a linear equation of modified Stefan-Boltzmann law given by [Lewin, van Paradijs & Taam \(1993\)](#):

$$L_{Edd} = 4\pi d^2 \xi F_{max} \quad (1)$$

where ξ is the anisotropy constant, which is taken as unity (assuming isotropic case), and F_{max} is the unabsorbed peak flux.

During the peak of the burst, peak flux attained $(4.2 \pm 0.1) \times 10^{-8}$ erg cm^{-2} s^{-1} and $(4.0 \pm 0.1) \times 10^{-8}$ erg cm^{-2} s^{-1} for burst 3 and burst 4 respectively. The expansion of the photospheric radius expansion is not evident as seen from the evolution of the spectral parameters. Taking Eddington luminosity $\sim 3.8 \times 10^{38}$ erg s^{-1} ([Kuulkers et al. 2003](#)), the upper limit of the source distance is estimated to be ~ 8.7 kpc.

We have also estimated the mass accretion rate at the surface of the neutron star. Depending on the local accretion rate, different thermonuclear ignition regimes can be determined. The accretion dominated luminosity assuming spherical accretion can be written

as (Galloway & Cumming 2006; Johnston 2020),

$$L = 4\pi d^2 F \zeta = \frac{z \dot{M} c^2}{(1+z)^3} \quad (2)$$

where \dot{M} is the mass accretion rate, ζ is the anisotropy factor, and F is the pre-burst flux. We have calculated the mass accretion rate using a pre-burst flux of 4.3×10^{-9} erg cm² s⁻¹ and a source distance of ~ 8.6 kpc.

$$\frac{(1+z)^3 4\pi d^2 F}{z \times c^2} \zeta = \dot{M} \quad (3)$$

$$\dot{M} = 6.6 \times 10^{-10} \times \frac{(1+z)^3 \times \zeta}{z} M_{\odot} \text{yr}^{-1} \quad (4)$$

For an isotropic case, $\zeta = 1$ and assuming $R = 10$ km, $M = 1.4 M_{\odot}$, we get gravitational redshift on the surface of the NS is $(1+z) = \left(1 - \frac{2GM}{c^2 R}\right)^{-\frac{1}{2}} \approx 1.3$ and the mass accretion rate is estimated to be $\dot{M} \approx 4.87 \times 10^{-9} M_{\odot} \text{yr}^{-1}$.

The change of burst properties of the individual system with the variation of accretion rates can be predicted by theoretical ignition models of hydrogen and helium-burning thermonuclear bursts. For stable hot CNO cycle hydrogen burning, the mass accretion rate is related to the Eddington mass accretion rate as $\dot{M} \geq 0.01 \dot{M}_{Edd}$ (Cumming 2004; Galloway & Cumming 2006; Galloway et al. 2008). In our study, we have found that $\dot{M} \approx 0.27 \dot{M}_{Edd}$, which is higher than the estimated rates by Cumming (2004) for stable CNO burning. At a lower accretion rate, $\dot{M} \leq 0.01 \dot{M}_{Edd}$, the temperature of the burning layer is too low for stable hydrogen burning and the unstable hydrogen ignition leads to ‘‘hydrogen-triggered’’ bursts (Cumming 2004; Galloway & Cumming 2006).

The α factor for bursts defined from the ratio of persistent and burst fluence using the relation (Galloway et al. 2008):

$$\alpha = \frac{F_{\text{persistent}} \times \Delta t_r}{E_{\text{burst}}} \quad (5)$$

where Δt_r is the recurrence time, $F_{\text{persistent}}$ is the bolometric flux of the persistent emission and E_{burst} is the burst fluence. The burst fluence is estimated from the time-resolved spectra and the $F_{\text{persistent}}$ is obtained using the convolution model `cflux` from the persistent spectra. One can categorize the sort of X-ray burst based on the theoretical value of α . For a pure helium burst, α is nearly 100–150, whereas α is close to 40 for a hydrogen-rich X-ray burst, assuming each X-ray burst burns through all accreted matter (Galloway et al. 2008). Earlier, the α was also estimated to be ~ 45 for MAXI J1816–195 using the Insight/HXMT and NICER observations (Bult et al. 2022; Chen et al. 2022). The mass accretion rate, burst duration, recurrence time, and the α value indicate that the bursts are powered by a hydrogen-rich environment (Lewin, van Paradijs & Taam 1993).

5 CONCLUSION

We study the timing and spectral properties of the newly discovered millisecond pulsar MAXI J1816–195 during the 2022 outburst using simultaneous *NuSTAR* and *NICER* observations. Multiple Type-I thermonuclear bursts are detected using *NuSTAR* and *NICER* observations and the burst profiles are modelled using a sharp linear rise and exponential decay function. The duration of each burst was around ~ 30 s, and a rise time of ~ 5 s were found. The burst is found up to 20 keV energy range using *NuSTAR*. The burst profiles evolved

significantly with energy, and a relatively long tail was observed in lower energy compared to higher energy. The faster decay of the burst in a higher energy range implies that the temperature decrease as the burst evolves. The hardness ratio shows significant evolution during the thermonuclear burst. The *NICER* soft X-ray count rate (0.4–3 keV) is enhanced by ~ 2.5 compared to the hard X-ray count rate (5–10 keV). Time-resolved spectroscopy is performed to study the evolution of different spectral parameters during the burst. The blackbody radius and flux increase towards the peak of the burst and show a trend to decrease in the decay phase of the burst. During the burst peak, the temperature and apparent emitting area of the blackbody reached a value of ~ 2.1 keV and ~ 12.5 km (for a source distance of ~ 8.6 kpc) respectively. Assuming the empirical Eddington limit, the upper limit of the source distance for isotropic burst emission is estimated to be ~ 8.7 kpc. The mass accretion rate is estimated to be $\approx 0.27 \dot{M}_{Edd}$, which implies stable burning of hydrogen in a hot CNO cycle.

ACKNOWLEDGEMENTS

We thank Dr. Tolga Guver for his useful suggestions, which help to improve the manuscript significantly. This research has made use of data obtained with *NuSTAR*, a project led by Caltech, funded by NASA, and managed by NASA/JPL, and has utilized the NUSTARDAS software package, jointly developed by the ASDC (Italy) and Caltech (USA). This research has made use of the *MAXI* data provided by RIKEN, JAXA, and the *MAXI* team. We acknowledge the use of public data from the *NuSTAR*, *NICER*, and *Fermi* data archives. We thank the *NuSTAR* SOC Team for making this ToO observation possible. We are also thankful to the *NICER* team for the continuous monitoring of the source.

DATA AVAILABILITY

The data used for this article are publicly available in the High Energy Astrophysics Science Archive Research Centre (HEASARC) at <https://heasarc.gsfc.nasa.gov/db-perl/W3Browse/w3browse.pl>.

REFERENCES

- Arnaud K. A., 1996, *ASPC*, 101, 17
- Bagnoli T., in’t Zand J. J. M., Patruno A., Watts A. L., 2014, *MNRAS*, 437, 2790
- Beauchamp I., Belvedere S., Hernandez M., Himes M., McCaffrey T., Sander-son K., Wolfe B., 2022, *The Astronomer’s Telegram*, 15481, 1
- Beri A. et al., 2019, *MNRAS*, 482, 4397
- Bhattacharyya S., 2010, *Adv. Space Res.*, 45, 949
- Bright J. et al., 2022, *The Astronomer’s Telegram*, 15484, 1
- Bult P. M. et al., 2022, *The Astronomer’s Telegram*, 15425, 1
- Bult P., et al., 2022, *ApJL*, 935, L32
- Chauhan J., Lohfink A., Bharali P., Mandal M., Draghis P., Pal S., Sanna A., 2022, *The Astronomer’s Telegram*, 15470, 1
- Chen Y.-P., Zhang S., Ji L., Zhang S.-N., Wang P.-J., Kong L.-D., Chang Z., et al., 2022, *ApJL*, 936, L21
- Cumming A., 2004, *Nuclear Physics B Proceedings Supplements*, 132, 435
- de Martino D. et al., 2022, *The Astronomer’s Telegram*, 15479, 1
- Devasia J., Raman G., Paul B., 2021, *NewA*, 83, 101479
- Degenaar N., Koljonen K. I. I., Chakrabarty D., Kara E., Altamirano D., Miller J. M., Fabian A. C., 2016, *MNRAS*, 456, 4256

Galloway D. K., Muno M. P., Hartman J. M., Psaltis D., Chakrabarty D., 2008, *ApJS*, 179, 360

Galloway D. K., & Cumming A. 2006, *ApJ*, 652, 559

Gendreau K. C. et al., 2016, in den Herder J.-W. A., Takahashi T., Bautz M., eds, *Proc. SPIE Conf. Ser. Vol. 9905, Space Telescopes and Instrumentation 2016: Ultraviolet to Gamma Ray*. SPIE, Bellingham, p. 99051H

Grindlay J., Gursky H., Schnopper H., Parsignault D. R., Heise J., Brinkman A. C., Schrijver J., 1976, *ApJL*, 205, L127

Harrison F. A. et al., 2013, *ApJ*, 770, 103

Johnston Z., 2020, preprint, arXiv:2004.00012

Jonker P. G., Galloway D. K., McClintock J. E., Buxton M., Garcia M., Murray S., 2004, *MNRAS*, 354, 666

Kennea J. A., Evans P. A., Negoro H., 2022, *The Astronomer's Telegram*, 15421

Kennea J. A., Evans P. A., Negoro H., 2022, *The Astronomer's Telegram*, 15467

Krimm H. A. et al., 2013, *ApJS*, 209, 14

Kuulkers E., Homan J., van der Klis M., Lewin W. H. G., Méndez M., 2002, *A&A*, 382, 947

Kuulkers E., et al., 2003, *A&A*, 399, 663

Lewin W. H. G., van Paradijs J., Taam R. E., 1993, *Space Sci. Rev.*, 62, 223

Liu Q. Z., van Paradijs J., van den Heuvel E. P. J. 2007, *A&A*, 469, 807

Li C., Zhang G., Méndez M., Wang J., Lyu M., 2021, *MNRAS*, 501, 168

Matsuoka M. et al., 2009, *PASJ*, 61, 999

Nath A., Sarkar B., Roy J., Misra R., 2022, arXiv, arXiv:2206.07450

Negoro H. et al., 2022, *ATel*, 15418

Penninx W., Damen E., Tan J., Lewin W. H. G., van Paradijs J., 1989, *A&A*, 208, 146

Pike S. N., et al., 2021, *ApJ*, 918, 9

Remillard R. A. et al., 2022, *AJ*, 163, 130

Schatz H., Rehm K. E., 2006, *NuPhA*, 777, 601

Strohmayer T., Bildsten L., 2003, arXiv, astro-ph/0301544

Tawara Y., et al., 1984, *ApJ*, 276, L41

van Paradijs J., 1978, *Nature*, 274, 650

van Paradijs J., Sztajno M., Lewin W. H. G., Trumper J., Vacca W. D., vander Klis M., 1986, *MNRAS*, 221, 617

Watts A. L., Maurer I., 2007, *A&A*, 467, L33

Wilms J., Allen A., & McCray R., 2000, *ApJ*, 542, 914

Worpel H., Galloway D. K., Price D. J., 2013, *ApJ*, 772, 94

Yu-Peng C., et al., 2022, arXiv, arXiv:2208.12124

Zdziarski A. A., Johnson W. N., & Magdziarz P., 1996, *MNRAS*, 283, 193

Zhang G., Méndez M., Altamirano D., Belloni T. M., Homan J., 2009, *MNRAS*, 398, 368

Zycki P. T., Done C., & Smith D. A., 1999, *MNRAS*, 309, 561

APPENDIX A: HR EVOLUTION

Here, we have shown the evolution of the hardness ratio of MAXI J1816–195 during thermonuclear bursts using *NuSTAR*.

This paper has been typeset from a $\text{\TeX}/\text{\LaTeX}$ file prepared by the author.

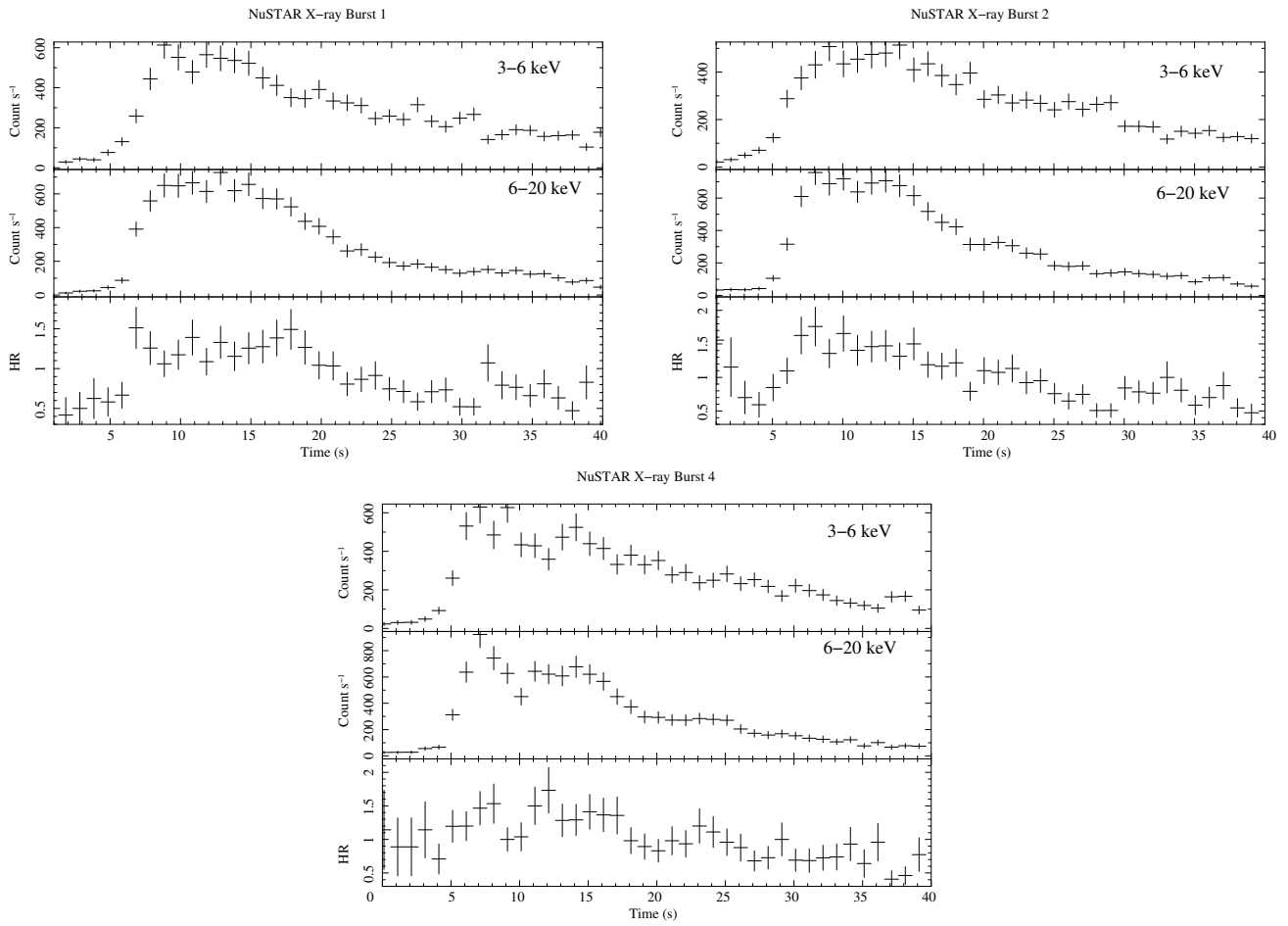


Figure A1. Evolution of hardness ratio of MAXI J1816-195 during thermonuclear bursts using *NuSTAR*. The first and second panels of each figure show the 1 s binned light curve in the energy bands of 3-6 keV and 6-20 keV, respectively. The bottom panel shows the variation of the hardness ratio (6-20 keV)/(3-6 keV) during bursts.

Table A1. Best-fitting parameters obtained through time-resolved analysis of *NICER* data for two bursts [XSPEC model TBabs \times bbodyrad]. We model *NICER* spectra of 23 bins for burst-3 and burst-4 from MAXI J1816–195 with the variation of the persistent spectrum during the Burst using the f_a method from Worpel, Galloway & Price (2013). The spectra from P2 to P18 are extracted for a time bin of 2 s and P19 to P24 are extracted for a time bin of 4 s. The hydrogen column density is fixed to $2.385 \times 10^{22} \text{ cm}^{-2}$ during the fitting of time-resolved spectra.

Burst phases	kT (keV)	Norm $_{kT}$	Non-thermal emission (f_a)	F_{Total}	$F_{bodyrad}$	$F_{Non-thermal}$	χ^2/dof
Burst No. 3							
P2	$1.0^{+0.20}_{-0.13}$	190^{+170}_{-103}	1.1 ± 0.2	7.0 ± 0.6	2.3 ± 0.5	4.7 ± 0.5	21.99/21
P3	$1.7^{+0.17}_{-0.14}$	189^{+55}_{-45}	1.5 ± 0.2	21.6 ± 0.8	15.1 ± 1.0	6.5 ± 0.6	53.49/56
P4	2.2 ± 0.13	208^{+35}_{-31}	1.7 ± 0.2	42.0 ± 1.3	34.3 ± 1.5	7.7 ± 0.7	90.34/94
P5	2.1 ± 0.13	227^{+39}_{-34}	1.6 ± 0.2	40.0 ± 1.3	32.7 ± 1.5	7.0 ± 0.7	96.85/90
P6	2.0 ± 0.12	261^{+44}_{-38}	1.6 ± 0.2	40.4 ± 1.2	33.2 ± 1.4	7.2 ± 0.7	98.09/95
P7	1.9 ± 0.12	273^{+46}_{-40}	1.6 ± 0.2	39.0 ± 1.2	32.0 ± 1.4	7.0 ± 0.7	99.89/92
P8	2.0 ± 0.12	236^{+41}_{-36}	1.5 ± 0.2	36.7 ± 1.2	30.0 ± 1.4	6.8 ± 0.7	85.51/87
P9	1.9 ± 0.13	233^{+47}_{-40}	1.4 ± 0.2	31.9 ± 1.1	25.8 ± 1.3	6.1 ± 0.6	81.95/77
P10	$1.9^{+0.17}_{-0.14}$	192^{+46}_{-39}	1.7 ± 0.2	30.3 ± 1.1	22.8 ± 1.4	7.5 ± 0.6	71.57/72
P11	1.7 ± 0.12	259^{+57}_{-49}	1.3 ± 0.2	24.3 ± 0.9	18.8 ± 1.0	5.6 ± 0.6	71.95/64
P12	1.7 ± 0.14	221^{+59}_{-49}	1.4 ± 0.2	23.2 ± 0.9	17.2 ± 1.1	6.0 ± 0.6	66.94/59
P13	1.6 ± 0.14	240^{+71}_{-58}	1.3 ± 0.2	20.4 ± 0.8	14.8 ± 1.0	5.6 ± 0.6	57.67/54
P14	1.4 ± 0.11	334^{+100}_{-81}	1.2 ± 0.2	17.6 ± 0.7	12.4 ± 0.8	5.1 ± 0.6	51.29/52
P15	1.4 ± 0.12	290^{+95}_{-76}	1.2 ± 0.2	16.5 ± 0.6	11.2 ± 0.8	5.3 ± 0.6	52.68/48
P16	$1.5^{+0.18}_{-0.14}$	191^{+71}_{-55}	1.4 ± 0.2	16.0 ± 0.7	10.0 ± 0.8	6.0 ± 0.6	41.77/44
P17	$1.4^{+0.15}_{-0.12}$	240^{+90}_{-69}	1.1 ± 0.2	13.8 ± 0.6	8.9 ± 0.7	4.9 ± 0.6	44.28/39
P18	$1.5^{+0.21}_{-0.15}$	176^{+79}_{-59}	1.2 ± 0.2	13.5 ± 0.6	8.3 ± 0.8	5.2 ± 0.6	42.19/37
P19	1.3 ± 0.09	246^{+71}_{-58}	1.1 ± 0.1	11.2 ± 0.3	6.5 ± 0.4	4.7 ± 0.4	66.79/68
P20	1.2 ± 0.10	231^{+89}_{-69}	1.0 ± 0.1	9.0 ± 0.3	4.6 ± 0.3	4.4 ± 0.4	59.51/55
P21	1.1 ± 0.10	271^{+129}_{-96}	1.0 ± 0.2	8.1 ± 0.3	3.5 ± 0.3	4.6 ± 0.4	48.21/51
Burst No. 4							
P2	2.1 ± 0.15	190^{+39}_{-34}	1.6 ± 0.2	34.0 ± 1.2	27.0 ± 1.4	7.0 ± 0.6	79.66/79
P3	2.1 ± 0.15	190^{+39}_{-34}	1.6 ± 0.2	34.0 ± 1.2	27.0 ± 1.4	7.0 ± 0.6	80.66/79
P4	2.1 ± 0.13	218^{+38}_{-33}	1.7 ± 0.2	40.1 ± 1.3	32.5 ± 1.5	7.6 ± 0.7	86.29/92
P5	2.1 ± 0.13	227^{+40}_{-35}	1.7 ± 0.2	40.3 ± 1.3	33.0 ± 1.5	7.4 ± 0.7	93.54/91
P6	2.1 ± 0.13	213^{+37}_{-32}	1.7 ± 0.2	38.9 ± 1.2	31.5 ± 1.4	7.3 ± 0.7	88.46/89
P7	2.0 ± 0.13	233^{+44}_{-39}	1.6 ± 0.2	36.8 ± 1.2	29.6 ± 1.5	7.2 ± 0.7	89.22/86
P8	2.0 ± 0.13	231^{+47}_{-40}	1.6 ± 0.2	34.8 ± 1.2	27.6 ± 1.4	7.2 ± 0.6	88.68/82
P9	1.7 ± 0.10	330^{+63}_{-55}	1.1 ± 0.2	27.2 ± 0.9	22.5 ± 1.1	4.7 ± 0.6	75.37/73
P10	1.8 ± 0.14	221^{+55}_{-46}	1.5 ± 0.2	25.9 ± 0.9	19.2 ± 1.2	6.8 ± 0.6	67.71/66
P11	1.7 ± 0.12	238^{+54}_{-46}	1.2 ± 0.2	23.0 ± 0.9	18.0 ± 1.0	5.1 ± 0.6	59.56/60
P12	$1.6^{+0.15}_{-0.12}$	246^{+69}_{-57}	1.3 ± 0.2	21.0 ± 0.8	15.5 ± 1.0	5.5 ± 0.6	61.87/56
P13	1.5 ± 0.12	262^{+73}_{-60}	1.1 ± 0.2	18.2 ± 0.7	13.4 ± 0.9	4.9 ± 0.6	53.64/51
P14	1.6 ± 0.13	203^{+59}_{-48}	1.4 ± 0.2	19.1 ± 0.7	12.7 ± 0.9	6.3 ± 0.6	57.10/51
P15	$1.5^{+0.15}_{-0.12}$	232^{+77}_{-61}	1.3 ± 0.2	16.8 ± 0.7	11.0 ± 0.8	5.7 ± 0.6	48.50/46
P16	1.3 ± 0.1	362^{+112}_{-90}	0.9 ± 0.2	14.1 ± 0.6	10.2 ± 0.6	3.9 ± 0.6	47.64/43
P17	1.3 ± 0.1	292^{+112}_{-86}	1.0 ± 0.2	12.5 ± 0.5	8.0 ± 0.6	4.5 ± 0.6	40.06/38
P18	$1.3^{+0.15}_{-0.12}$	240^{+100}_{-76}	1.1 ± 0.2	12.0 ± 0.5	7.2 ± 0.5	4.8 ± 0.6	40.14/35
P19	1.2 ± 0.1	285^{+76}_{-65}	0.9 ± 0.1	10.4 ± 0.3	6.3 ± 0.3	4.1 ± 0.4	65.57/64
P20	$1.2^{+0.10}_{-0.05}$	251^{+84}_{-67}	0.9 ± 0.1	9.2 ± 0.3	5.1 ± 0.3	4.1 ± 0.4	62.93/57
P21	1.0 ± 0.08	293^{+118}_{-91}	1.0 ± 0.2	7.7 ± 0.2	3.5 ± 0.2	4.2 ± 0.4	53.25/49
P22	1.0 ± 0.10	268^{+136}_{-99}	0.9 ± 0.2	6.6 ± 0.2	2.6 ± 0.2	4.0 ± 0.4	45.39/42
P23	0.9 ± 0.09	291^{+160}_{-116}	0.9 ± 0.2	6.1 ± 0.2	2.2 ± 0.2	4.0 ± 0.4	44.49/40
P24	$0.8^{+0.12}_{-0.08}$	355^{+259}_{-177}	0.9 ± 0.2	5.6 ± 0.2	1.8 ± 0.2	3.8 ± 0.4	39.28/35

* : All the errors are 90% significant and calculated using the MCMC approach in XSPEC

** : All the flux values are unabsorbed and calculated for the energy band 0.1–10 keV and in the unit of $10^{-9} \text{ ergs cm}^{-2} \text{ s}^{-1}$